Collimation of Fast Electrons in Critical Density Plasma Channel

Tomoyuki IWAWAKI, Hideaki HABARA, Sophie BATON[1], Kiyoshi MORITA, Julien FUCHS[1],
Sophia CHEN[1], Motoaki NAKATSUTSUMI[1,2], Christophe ROUSSEAUX[3], Francesco FILIPPI[4],
Wigen NAZAROV[5] and Kazuo A. TANAKA

Graduate School of Engineering, Osaka University, 2-1 Yamada-oka, Suita, Osaka 565-0871, Japan
[1]*LULI, CNRS -Ecole Polytechnique -Université Pierre et Marie Curie -CEA, 91128 Palaiseau, France*
[2]*European X-Ray Free-Electron Laser Facility (XFEL) GmbH, Germany*
[3]*CEA, DAM, DIF, F-91297 Arpajon, France*
[4]*La SAPIENZA, University of Rome, Dip. SBAI, 00161 Rome, Italy*
[5]*School of Chemistry, University of St. Andrews, North Haugh, St. Andrews, Fife KY16 9ST, Scotland, UK*

Significantly collimated fast electron beam with a divergence angle 10° (FWHM) is generated through the interaction of ultra-intense laser light with a uniform critical density plasma in experiments and 2D PIC simulations. In the experiment, the uniform critical density plasma is created by ionizing an ultra-low density foam target. The spacial distribution of the fast electron is observed by Imaging Plate. 2D PIC simulation and post process analysis reveal magnetic collimation of energetic electrons along the plasma channel.

In the fast ignition (FI) of inertial confinement fusion [1], the external heating laser has to transfer the energy to the high density core plasma that is surrounded by large corona plasma [2]. Super-penetration is one of the method to heat the core plasma [3]. In this method, the imploded plasma is irradiated directly by the ultra-intense laser pulse (UILP). The UILP propagates into the corona region with relativistic self-focusing (RSF), resulting in increase of the laser intensity. When the enforced UILP arrives the critical density region, relativistic induced transparency (RIT) allows the pulse to propagate until higher relativistic critical density. Eventually, the laser energy is transferred to fast electrons at the critical or overcritical density interface [4]. In our previous work, the divergence angle of the fast electron beam was observed 33° (FWHM) when the UILP penetrated into several tens μm overdense plasma [5]. This divergence angle is significantly narrower than that obtained at the plain target, 66° (FWHM). However, the detailed physical mechanism has not been understood.

In this letter, therefore, we investigate the characteristics of the fast electron generated around critical density plasmas. For the purpose, we use a small capillary tube filled with ultra low-density plastic foam. The foam is heated and ionized by another nsec infrared laser [6]. After the ionization, an UILP (10^{19} W/cm^2) irradiates and propagates in the plasma. In the electromagnetic field of the UILP, electrons are accelerated toward the laser direction via $J \times B$ heating, B-loop acceleration, and betatron resonance acceleration [7–9]. The spatial distribution of the ac-

celerated electrons is observed using an imaging plate (IP) stack. The distributions indicate the divergence angle of the fast electrons is $11 \pm 2°$ (FWHM). This angle is around a quarter of the one (35~65° (FWHM)) measured in case of the standard foil target [5, 10, 11]. 2D PIC simulation also produces this narrow electron beam divergence. To understand the physical mechanism, the motion of electrons that follows Lorentz force is calculated in the magnetic field obtained from the simulation. The results indicate that the structure and strength of magnetic field in the plasma channel strongly collimate the electrons that have energy over a few MeV.

We performed the experiment at the ELFIE facility at LULI, École Polytechnique using two laser beams. The setup is shown in Fig. 1. The ultra-low density plastic foam ($C_{15}H_{20}O_6$) is filled in polyimide tube. The length, wall thickness, and inside diameter of the tube are 300 μm, 20 μm, and 254 μm respectively. The foam density is 5 mg/cc that corresponds to the critical density (10^{21}/cc) when the foam becomes plasma. The thin Cu foil (0.7 μm thick) is attached to one side of the tube to generate X-rays burst that heats the foam. The burst is produced by the interaction with the foil and the infrared ($\lambda = 1.057$ μm) laser pulse (60 J / 600 ps) at focused intensity of 10^{14} W/cm^2 [6]. The X-rays burst heats the foam material up to a few tens eV and creates uniform critical density plasma 1 nsec after the long pulse laser irradiation according to the 1D hydro-radiative simulation, CHIC [6]. The micro-structure of the foam may be vanished and the plasma density should be homogenized within a few tens ps given by dividing the
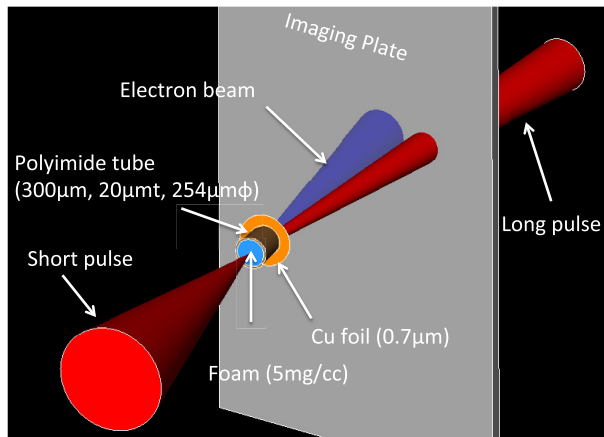
Fig. 1 Schematic of experimental setup. A thin Cu foil (0.7 μm) is irradiated by a long (600 psec) pulse to generate X-ray burst that ionizes the entire foam target and creates an uniform critical density plasma. An UILP is focused at the surface of the open side of the tube target.
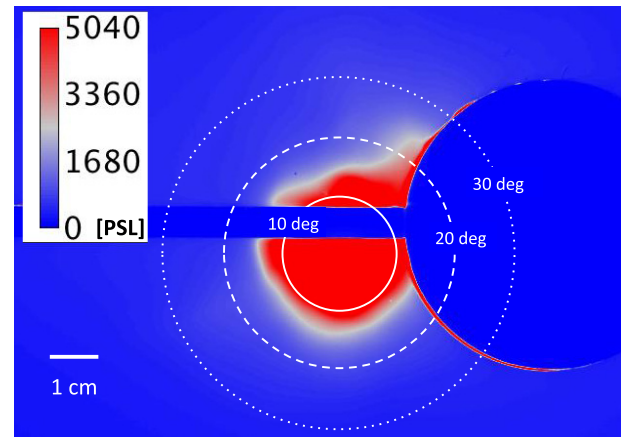

Fig. 2 Typical results of electron beam divergence observed on IP stack from 135 mm behind the target. The solid, dashed, and dotted lines indicate divergence angles of 10°, 20°, and 30° respectively.

structure size by the sound speed. The density of the solid and ionized foam are measured and checked by performing 2D X-ray radiography [12].

After the foam becomes uniform critical density plasma, the UILP is focused on the surface of the open side of the tube (the blue surface in Fig. 1). Here, the time delay between fsec and nsec pulses is set to be 800 ps referring to the simulation and the X-ray radiography. The wavelength and time duration of the pulse is 1.057 μm and 300 fs time. The off-axis parabola $f/3$ focuses the laser to a 10 μm diameter spot producing an intensity of 10^{19} W/cm² in vacuum. The SR Imaging plate (IP) that observe the emission pattern of the electron beam is set at 135 mm behind the target. This IP is covered with an Al foil (7 μm thickness) to protect the IP from lights. Based on the continuous-slowing-down approximation (CSDA) range calculation [13], electrons with energies over 25 keV can be observed through the Al foil.

Figure 2 shows typical electron beam pattern on the IP. The blue circle and line correspond to the entrance of the long pulse beam to the target and the entrance to other detector (not presented in the paper), respectively. In order to observe the electron beam as emitted from the target but avoiding the overlap with the hole for the long pulse laser on the IP, the tube target was tilted in the horizontal plane with respect to the short and long pulse beam axis by 7° as shown in Fig. 1. It is clearly shown that the electron beam is significantly collimated compared to that obtained from standard foil targets (35~65° (FWHM)) [5, 10, 11]. Using gaussian fitting to the electron distribution, the divergence angle is estimated to be 11° ± 2° (FWHM). This kind of narrow electron beam was also observed in the other shots. The pointing and the divergence of the beam were estimated to be 2.7 ± 0.9° and 10.3 ± 2.2°. On the IP, signals from X-rays and protons could be also included. How-

ever, the signal intensity of the X-rays should be much weaker than that from electrons considering the average atomic number ($Z = 3.7$) and electron density ($1N_c$) [14]. The energetic protons are mainly generated in the radial direction of the plasma channel via Ponderamotive force in this laser intensity and plasma density parameters [9]. Therefore the IP would not be able to observe high energy proton. Even if the small portion of proton would arrive on the IP, the divergence angles is bigger than the observed angles of 11° (FWHM) because our PIC simulation (the details are shown in the next section) indicates also large divergence angle, 138°. Thus, the narrow signal on the IP indicates the electrons distribution.

2D PIC simulation (FISCOF [15]) using the experimental configurations also indicates the narrow divergence of the electrons. In the simulation, the critical density plasma is set in the region $0 \, \mu m \leq X \leq 60 \, \mu m$ and $-70 \, \mu m \leq Y \leq 70 \, \mu m$ and the UILP propagates along X axis. The plasma size is smaller than the actual target due to the calculation capacity. But this simulation can model the experimental result since the laser propagates up to 40 μm in depth in this simulation. Referring to the CHIC calculation, preformed plasma is attached on the surface of the critical density plasma from $X = 0 \, \mu m$ ($1 \, N_c$) to $X = -5 \, \mu m$ ($0.1 \, N_c$). The UILP comes from the surface of $X = -7 \, \mu m$ with the spot size of 10 μm (Gaussian shape). The center of the spot is located at $Y = 0 \, \mu m$. The pulse duration is 300 fs (FWHM) with Gaussian shape. The maximum intensity is set to be 3×10^{19} W/cm². Fast electrons are observed at 10 μm from the rear surface of the plasmas ($X = 70 \, \mu m$). Angular distribution of the observed fast electrons (> 25 keV) is shown in Fig. 3 (a). The estimated divergence angle is 12° (FWHM), which corresponds to the experimental result. The electron energy spectrum is shown in Fig. 3 (b). Here we note that 90% of the electrons carried energies of over 1 MeV. In this simulation, we also
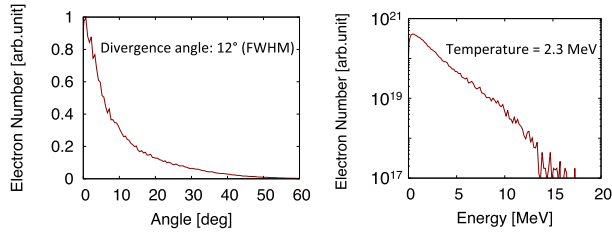
Fig. 3   Electron beam divergence (a) and spectrum (b) that detected at the observation line which separated 10 μm from the target rear surface in PIC simulation.
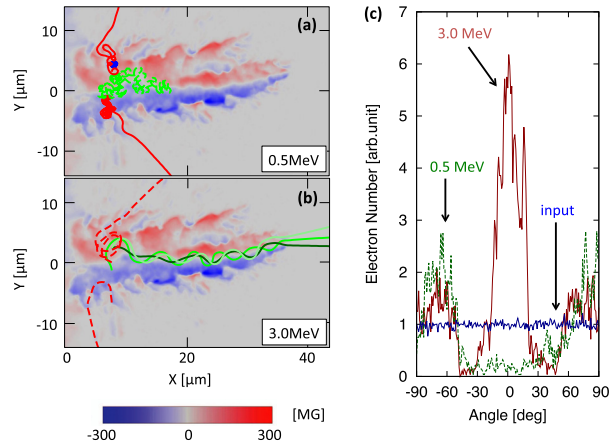

Fig. 4   Typical magnetic field generated in the critical density plasma at 600 fs and electrons tracks (lines) with energies 0.5 MeV (a) and 3.0 MeV (b). The maximum laser intensity reaches the critical density surface at 400 fs. (c) The angular distribution of fast electrons arrive at the simulation boundaries. The horizontal axis indicates angle from the X axis. These electron energies are 3.0 MeV (red solid) and 0.5 MeV (green dashed), respectively. The blue solid line indicates just the input distribution.

observed protons in the plasma. The average energy, cut off energy, and divergence angle are 0.5 MeV, 5 MeV and 138° (FWHM), respectively. Assuming the conversion efficiency from laser to proton energy of 1% and using proton sensitivity for IP [16], signal intensity on the IP from protons are 20 times smaller than that from electrons [17].

Since the simulation result reproduces the experimental results qualitatively, we proceed to find the collimation mechanism using the magnetic field in the simulation that is well known to function as an electron collimator [18–20] or scatterer [21, 22]. Figures 4 (a) and (b) show typical magnetic field structure taken at the timing of 600 fs as calculated by the PIC code. At 400 fs, the maximum laser intensity arrives at the critical density surface. This field is created by electron current propagating toward X direction in the plasma channel. The outside magnetic field is neutralized by the return currents which flow the boundary of the channel [23]. The strength of the field has a peak at 600 fs with ~300 MG and the time duration is 800 fs

(FWHM). The length develops with the laser propagation up to ~40 μm at 650 fs. The vertical size corresponds to the spot size of the incident laser pulse ~10 μm.

To understand how the magnetic field affects on the collimation, we introduce test electrons. The electrons has a uniform angular distribution from −180° to 180° against X direction with a mono energy. The initial source is located at $X = 8$ μm and -5 μm $\leq Y \leq 5$ μm. The motions of the electrons in this magnetic field are calculated using Lorentz force, $\boldsymbol{F} = -e(\boldsymbol{v} \times \boldsymbol{B})$. The tracks of 0.5 MeV electrons are shown by lines in Fig. 4 (a). A number of electrons stagnate in the strong magnetic field (blue and green dashed lines). In this calculation, 42% of the electrons are trapped in the field. Even if they escape from the field, it is difficult to propagates X direction at small angle due to the interruption of the field (red solid lines). On the other hand, high energy electrons propagate X direction with good collimation. The tracks of 3.0 MeV electrons are shown by lines in Fig. 4 (b). A number of electrons are bound around the field and propagate forward direction at small angle (green lines). Even if they are almost trapped, they can escape from the field due to the high electron energy (red dashed lines). When these electrons pass the simulation boundary, direction angles of the electrons are recorded. Red solid and green dashed lines in Fig. 4 (c) indicate the angular distributions of the electrons with the energy 3 MeV and 0.5 MeV, respectively. In the low energy (0.5 MeV) case, the electron number between −45° and 45° significantly decreases since the magnetic field prevents the electrons from forward propagation. This result indicates the magnetic field works as scatterer for the low energy electron. On the contrary, in the high energy (3.0 MeV) case, the electron number between −20° and 20° significantly increases since a number of electrons are bound around and propagates in the magnetic field. This result indicates the magnetic field works as collimator for the high energy electron. The reason may be explained using the Larmor radius represented as $r_L = m_e c^2 \sqrt{\gamma^2 - 1}/(eB)$. Here, γ and m_e are the electron Lorenz factor and the electron mass, respectively. Since the radius becomes small when the electron energy decreases, the low energy electrons are trapped in the strong magnetic field if the radius is much smaller than that of the magnetic field. On the other hand, when the energy is high enough, the electrons are not trapped but are bound around the field and propagate forward with good collimation. According to the further calculation, we found that electrons with energy over a few MeV were collimated by the strong magnetic field (~100 MG). After passing through the magnetic field, both the scattered and collimated electrons propagate in the critical density plasma. When these electrons arrive at the rear side of the target, the sheath potential is exited at the rear surface. Generally, electrons which have energy under the average energy can not escape from the target due to the sheath potential. Therefore, only collimated electrons with over a few MeV

escape the target and are observed on the IP in this experiment considering the observed electron temperature in Fig. 3 is 2.3 MeV.

Based on the result, we discuss about the fast electron collimation in further over dense plasmas. The magnetic field working as collimator is created by the forward going electron current represented as, $B(r) = (2\pi/c)en_e v_e r$. Here, n_e, v_e, and r are the background electron density, the electron flow speed, and the radius of the plasma channel. Using the observed flow speed in the simulation $0.18\,c$ and the channel radius $5\,\mu m$, the maximum strength of the magnetic field in the critical density plasma is estimated to be 270 MG, which corresponds to the observed strength 300 MG in the previous simulation. Assuming the same flow speed when the UILP penetrates 10 times critical density plasma with the diffraction limit ($r = 0.5\,\mu m$), the maximum strength of the magnetic field is also estimated to be 270 MG. This strong magnetic field could also collimate significantly the fast electron beam.

In this letter, significantly collimated electron beam with a divergence angle 11° has been observed when the ultra-intense laser pulse at $10^{19}\,W/cm^2$ irradiates the uniform and long critical density plasma. 2D PIC simulation also indicates the narrow divergence angle. Post process analysis using magnetic field taken from the 2D PIC simulation reveal the strength and structure of the magnetic field in the plasma channel collimates electrons with energy over a few MeV. Therefore, we conclude the narrow electron beam divergence is caused by the strength and structure of the magnetic field in the plasma. Similar collimation mechanisms have been reported in cone wire target [18], target surface coiling [24], resistivity controlled target [19] and preformed magnetic field structure [20]. But the difference in our case, the strong magnetic field for the collimation is generated along the plasma channel in critical or over dense plasma. In addition, the generated electron beam has a high density and low temperature comparing with those from wake field and surface waves accelerations [25–28]. This collimated and high intensity electron beam over a few MeV may be use for the direct heating of high density core in the Super-penetration [29].

[1] M. Tabak et al., Phys. Plasmas **1**, 1626 (1994).
[2] R. Kodama et al., Phys. Plasmas **8**, 2268 (2001).
[3] K.A. Tanaka et al., Phys. Plasmas **7**, 2014 (2000).
[4] A.L. Lei et al., Phys. Rev. E **76**, 066403 (2007).
[5] T. Tanimoto et al., J. Phys.: Conf. Ser. **112**, 022095 (2008).
[6] R.J. Mason et al., Phys. Plasmas **5**, 211 (1998).
[7] W.L. Kruer and K. Estabrook, Phys. Fluid **28**, 430 (1985).
[8] A. Pukhov and J. Meyer-ter-Vehn, Phys. Plasmas **5**, 1880 (1998).
[9] A. Pukhov, Z.-M. Sheng and J. Meyer-ter-Vehn, Phys. Plasmas **6**, 2847 (1999).
[10] J.S. Green et al., Phys. Rev. Lett. **100**, 015003 (2002).
[11] Y.T. Li et al., Phys. Rev. E **69**, 036405 (2004).
[12] S. Chen et al., preparation for submission to Phys. Plasmas.
[13] National Institute of Standards and Technology, Physical Means. Laboratory, ESTAR, http://physics.nist.gov/PhysRefData/Star/Text/ESTAR.html
[14] T. Yabuuchi et al., Phys. Plasmas **14**, 040706 (2007).
[15] H. Sakagami and K. Mima, Proc. of 2nd Int. Conf. Inertial Fusion Sciences and Applications, Kyoto, 2001, 380-383 (Elsevier, 2002).
[16] T. Bonnet et al., Rev. Sci. Instrum. **84**, 013508 (2013).
[17] K.A. Tanaka et al., Rev. Sci. Instrum. **76**, 013507 (2005).
[18] R. Kodama et al., Nature **432**, 1005 (2004).
[19] S. Kar et al., Phys. Rev. Lett. **102**, 055001 (2009).
[20] R.H.H. Scott et al., Phys. Rev. Lett. **109**, 015001 (2012).
[21] A. Debayle et al., Phys. Rev. E **82**, 036405 (2010).
[22] V.M. Ovchinnikov et al., Phys. Rev. Lett. **110**, 065007 (2013).
[23] A. Pukhov and J. Meyer-ter-Vehn, Phys. Rev. Lett. **76**, 3975 (1996).
[24] H. Habara et al., Phys. Rev. Lett. **97**, 095004 (2006).
[25] T. Tajima and J.M. Dawson, Phys. Rev. Lett. **43**, 267 (1979).
[26] N. Nakanii et al., Appl. Phys. Lett. **93**, 081501 (2008).
[27] N. Naseri, S.G. Bochkarev and W. Rozmus, Phys. Plasmas **17**, 033107 (2010).
[28] L. Willingale et al., Phys. Rev. Lett. **106**, 105002 (2011).
[29] T. Matsuoka et al., Plasma Phys. Control. Fusion **50**, 105011 (2008).